applied sciences

MDPI

Article

Analysis of Underwater Single-Photon LiDAR Signals: A Comprehensive Study on Multi-Parameter Coupling Effects

Ceyuan Wang [1,2], Shijie Liu [1,*], Shouzheng Zhu [1,*], Wenhang Yang [1], Chenhui Hu [1], Yuwei Chen [3], Chunlai Li [1,4] and Jianyu Wang [1,4]

[1] Hangzhou Institute for Advanced Study, University of Chinese Academy of Sciences, Hangzhou 310024, China; wangceyuan23@mails.ucas.ac.cn (C.W.); yangwenhang22@mails.ucas.ac.cn (W.Y.); huchenhui@ucas.ac.cn (C.H.); lichunlai@mail.sitp.ac.cn (C.L.); jywang@mail.sitp.ac.cn (J.W.)
[2] University of Chinese Academy of Sciences, Beijing 100049, China
[3] Advanced Laser Technology Laboratory of Anhui Province, Hefei 230037, China; chinaway.fgi@gmail.com
[4] Shanghai Institute of Technical Physics, Chinese Academy of Sciences, Shanghai 200083, China
* Correspondence: liushijie@ucas.ac.cn (S.L.); zhushouzheng@ucas.ac.cn (S.Z.)

Featured Application

This work explores underwater single-photon LiDAR (SPL) signal dynamics under multi-parameter coupling, providing key technical support for marine resource exploration, environmental monitoring, and national security. With sub-nanosecond ranging stability and strong anti-attenuation capability, it enables high-precision seabed target detection in turbid waters, laying a foundation for lightweight SPL deployment on autonomous underwater vehicles.

Abstract

Underwater laser signal attenuation challenges conventional detection, while single-photon LiDAR (SPL) with high sensitivity shows promise. Existing underwater SPL studies primarily focus on isolated parameters, while the coupled effects of environmental and system parameters remain insufficiently investigated. In this work, a 532 nm underwater SPL system was developed to systematically explore multi-parameter coupling mechanisms in laboratory water tanks, including air and three turbidity levels, three detection distances, four laser energy levels, three integration times, and seven targets. This provides quantitative guidance for optimizing SPL systems in complex underwater environments. The results show that the SPL system maintained sub-nanosecond ranging precision, with the standard deviation (SD) of the ranging measurement at 50 cm being 0.0117 ns under low turbidity (0.11 m^{-1}) with 50% laser energy, while under high turbidity (4.2 m^{-1}) conditions, it increased to 0.0338 ns. At 100 cm, the SD was 0.0187 ns in low turbidity and rose to 0.0877 ns in high turbidity. Furthermore, the inversion error of the highly reflectivity minerals was kept within 3%, and the inversion value of reflectivity decreased exponentially with the increase of turbidity. Moreover, there is an important discovery for the phenomenon of the forward shift of photon flight time detected for highly reflectivity targets. Longer integration times effectively enhanced the signal-to-noise ratio (SNR) under severe attenuation, whereas excessive laser energy risked detector saturation. These findings provide a systematic characterization of how multifactor coupling governs SPL signal dynamics. The results validate the feasibility of SPL for complex underwater detection and offer theoretical insights and technical guidance for future marine applications in resource exploration, environmental monitoring, and national security.

Keywords: LiDAR; TCSPC; SPAD; underwater optical detection; signal analysis

Received: 7 January 2026
Revised: 31 January 2026
Accepted: 31 January 2026
Published: 2 February 2026

1. Introduction

The ocean plays a crucial role in global ecology and resource exploration. However, effective underwater optical detection remains challenging due to strong attenuation and scattering. These resources include polymetallic deposits such as manganese nodules and cobalt-rich crusts located on the seafloor, as well as oil and gas reserves within marine sediments [1], as well as bioactive compounds with pharmaceutical value. The total reserves of these resources are believed to far exceed those on land. Consequently, underwater target detection and resource exploration have become critical technologies supporting marine development and environmental protection [2].

Traditional sonar systems typically offer resolutions in the range of centimeters to decimeters depending on the frequency—for example, common mid-frequency sonar (10–100 kHz) used in seabed surveys achieves a resolution of 10–50 cm, while low-frequency sonar (<10 kHz) for long-range detection may only reach 50 cm–100 m—whereas single-photon LiDAR (SPL) techniques can achieve millimeter-level precision. Specifically, the SPL system in this study exhibits a ranging error of only 1.76 μm at 50 cm distance under low turbidity, and even in high turbidity (4.22 m^{-1}) at 200 cm, the error remains <17 μm. This sub-millimeter to tens-of-microns accuracy is essential for detailed identification of small seabed targets like manganese nodules, where distinguishing individual nodules or subtle surface features requires precision far beyond traditional sonar's capabilities; and conventional LiDAR techniques typically require high=energy laser pulses to counteract water attenuation. This results in complex systems that may also disturb marine life. The SPL, by leveraging the high sensitivity of a single-photon avalanche diode (SPAD) [3,4], enables long-range underwater detection using low-energy pulses in the microjoule range. With its compact size, high attenuation resistance, and low power requirements, SPL has been successfully employed in spaceborne remote sensing applications [5–7]. SPL systems can achieve long-range and high-resolution detection using low-pulse-energy lasers and small-aperture optics, which facilitates lightweight and highly integrated designs suitable for deployment on underwater platforms such as autonomous underwater vehicles. Single-photon detection has also been explored in atmospheric remote sensing [8–11], distributed fiber-optic sensing [12,13], and underwater target imaging [14]. In recent years, SPL has been increasingly applied in oceanic LiDAR systems [15–18]. Existing studies in underwater SPL have demonstrated its feasibility for 3D imaging [19] within blind zones, depth-resolved ocean observations using shipborne systems [20], and detection of aquatic phytoplankton profiles [21]. Some have even achieved three-dimensional reconstructions at distances up to 3 m underwater using SPL sensor arrays [22]. In addition, the system modules used in existing studies are not compact enough and have insufficient resolution. In contrast, this work uses a small-aperture receiver and an 8ps resolution data acquisition module to ensure the miniaturization and high-precision sampling of the laser radar system; most of the existing research uses high-power lasers, which pose a potential threat to underwater environments and organisms. However, the laser pulse energy in this article is only 2 μJ.

Despite these advances, underwater SPL research remains at an early stage. Existing studies have primarily examined isolated variables, such as turbidity, target reflectivity [23], or laser energy, all under simplified experimental conditions. In real aquatic environments, however, environmental parameters such as turbidity, bubbles, suspended particles, target reflectivity, and system parameters such as laser energy, integration time, and detector sensitivity interact in a coupled manner, producing nonlinear signal dynamics. Current research lacks systematic investigations into these multifactor interactions, as well as quan-

titative assessments of ranging accuracy and reflectance inversion under realistic conditions. Addressing these gaps is essential for optimizing SPL system design and advancing its deployment in practical marine environments. In this study, with the underwater SPL system, we constructed a controlled multi-parameter environment within a 4 m test tank using a full-factorial design, and in order to simulate real underwater interference, suspended particles and bubbles [24] were also added to enhance the actual correlation. Signal features, ranging performance, and reflectance errors were comprehensively analyzed to uncover the underlying coupling effects, which multi-parameter coupling refers to experimentally observed non-additive interaction effects among turbidity, laser energy, and integration time, rather than independent or linearly superimposed parameter influences. A coupling effect is identified when the effectiveness of one parameter varies significantly with the level of another parameter, resulting in nonlinear sensitivity trends that cannot be explained by isolated parameter analysis. Unlike previous studies that focused on isolated variables, this work reveals the nonlinear coupling mechanisms governing underwater SPL performance. Specifically, we quantified the trade-off between laser energy and backscatter saturation in turbid waters and established an exponential decay model for reflectivity inversion, identifying a distinct 'time-shift' phenomenon critical for high-precision seabed resource exploration. For example, for the clear influence of system and environmental parameters, turbidity was the dominant factor driving signal attenuation, while target reflectivity governed echo intensity and ranging accuracy. Furthermore, integration time significantly improved the signal-to-noise ratio (SNR) in high attenuation conditions, whereas excessive laser energy risked SPAD saturation. Systematically investigating these interactions enhances our understanding of underwater photon propagation. This research provides theoretical insights and practical guidance for parameter optimization and supports the deployment of SPL systems in underwater exploration.

This paper is organized as follows. Section 2 introduces the SPL system architecture and parameter design, as well as the methodology for reflectance calculations and ranging accuracy assessments. Section 3 describes the experimental design, including target selection, environmental modeling, and parameter settings. Section 4 analyzes the experimental results, including signal characteristics, ranging errors, and reflectance inversion performance, followed by the concluding remarks in Section 5.

2. System and Methods

2.1. System Configuration

In this study, we primarily investigate the response of the SPL system under various underwater conditions and evaluate the influence of coupled factors on its performance. The SPL system employed is capable of high-sensitivity detection and consists of a 532 nm pulsed laser (Brillouin Laser, Shanghai, China), a SPAD (Excelitas, SPCM-AQRH-14-FC, Pittsburgh, PA, USA), a time-correlated single-photon counting (TCSPC) module (Time Tagger Ultra, Swabian Instruments, Stuttgart, Germany), and a reflective collimator with >96% reflectivity and a 23.5 mm aperture. Optical power calibration was performed using a Thorlabs PM400 power meter (Newton, NJ, USA), while data acquisition and system control were managed via a dedicated PC. The 532 nm wavelength was selected because it falls within the 'blue-green window' of the underwater optical spectrum, where water exhibits minimum absorption and scattering. This wavelength ensures maximum penetration depth and is supported by high-performance pulsed laser technology suitable for sub-nanosecond timing. The laser produces 1 ns pulses at a 45 kHz repetition rate with 2 μJ pulse energy, and the emitted energy was tuned using a variable attenuator wheel placed at the laser output, ensuring alignment between the filter center height and the laser beam axis. A collimator with a divergence angle of 0.5 mrad was employed to maintain a narrow beam

for high-ranging accuracy. Backscattered photons from targets were collected by a 50.8 mm focal length reflective collimator and coupled into a 105 µm core multimode fiber (MMF), which directed the signal to the SPAD. The system's narrow field of view (FOV) minimized background noise, while a 25.4 mm diameter bandpass filter centered at 532 ± 0.6 nm was used to further suppress ambient light. Time-resolved photon histograms were constructed using an 8 ps resolution time-to-digital converter. The overall structure of the unpackaged SPL system is illustrated in Figure 1. A summary of the key system parameters is provided in Table 1.

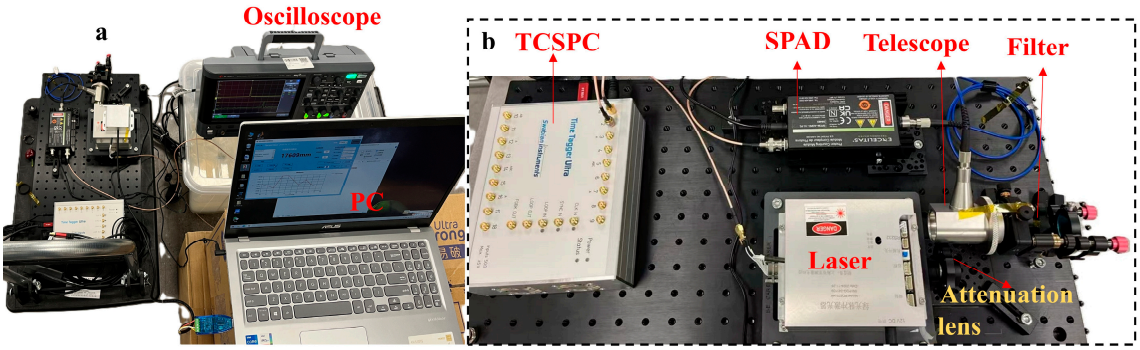

Figure 1. Schematic of underwater SPL system architecture: (**a**) overview of the SPL system; (**b**) main functional components.

Table 1. Key parameters of the SPL system.

Device	Parameter	Value
laser	Wavelength	532 nm
	Pulse duration	1 ns
	Pulse energy	2 µJ
	Pulse repetition rate	45 kHz
	Radius of laser beam	2 mm
	Divergence angle	0.5 mrad
Receiver	Focal length	50.8 mm
	Mode-field diameter of the MMF	105 µm
	Effective aperture	22.4 mm
	Bandwidth of the filter	5 nm
	Center wavelength	532 nm
SPAD	Detection efficiency	65%
	Dark count rate	100 cps
	Dead time	20 ns
	Bin width	8 ps
	Ranging Precision	50 ps (Air)/ 100–200 ps (Underwater)

2.2. Underwater LiDAR Equation

The operating principle of underwater LiDAR is based on the transmission of laser pulses through water and their interaction with submerged targets. During propagation in the water column, photons undergo absorption and scattering. The backscattered photons from the target are then detected by the SPAD and counted using the TCSPC module. To quantitatively express the received power P_r as a function of system parameters,

target properties, and water attenuation, we adopt the classical hard-target underwater LiDAR model:

$$P_r(Z,\lambda) = P_t(\lambda) \cdot A_r \cdot O(Z) \cdot \frac{\rho_b(\lambda)}{\pi} \cdot \frac{\eta_t(\lambda)}{Z^2} \cdot \exp(-2k_{lidar}(\lambda) \cdot Z) \quad (1)$$

where P_t is the laser output power, A_r is the receiver's effective aperture, O is the geometric overlap factor, $\rho_b(\lambda)$ is the target reflectance at wavelength λ, η_t is the total optical efficiency of the system, k_{lidar} is the water attenuation coefficient (including absorption and scattering), Z refers to the distance from the laser entering the water body to the underwater target, and the zero point is the laser exit point of the lower reflector.

Equation (1) is derived based on a hard-target underwater LiDAR model with exponential attenuation and geometric overlap. Under highly turbid conditions, multiple scattering, volume backscatter, and forward scattering may violate the assumptions of this simplified model. In this work, Equation (1) is employed as an effective comparative framework for controlled laboratory experiments rather than a full radiative transfer solution.

It is worth noting that the ranging accuracy differs significantly between air and underwater environments. In air, the system maintains a high-ranging stability with a standard deviation (SD) of approximately 11 ps. In underwater environments, the propagation velocity of the laser pulse decreases (v = c/1.33), and suspended particles induce multiple scattering. This scattering effect causes temporal broadening of the return pulse, thereby increasing the timing jitter. Our experimental results (detailed in Section 4.4) indicate that the ranging SD ranges from 0.0117 ns in low turbidity (0.11 m^{-1}) to 0.0877 ns in high turbidity (4.22 m^{-1}), demonstrating the system's sub-nanosecond stability even under strong scattering conditions.

2.3. Reflectance Retrieval Method

Reflectance estimation was conducted through comparative experiments using six types of mineral samples and a reflective plate. The given reflective plate is a circular plate with a diameter of 2 cm, used as a Lambertian body, and its reflectivity for a 532 nm laser is 0.97. If the received photon counts of each target are compared under the same conditions, and the reflectivity of the reflective plate is known, the reflectivity of the target R_{ore} is calculated as follows:

$$R_{ore} = \frac{I_{ore}}{I_{plate}} \cdot R_{plate} \quad (2)$$

where I_{ore} and I_{plate} denote the measured photon counts from the mineral sample and reflective plate, respectively.

To improve the accuracy of reflectivity, a multispectral camera [25] with a wavelength range of 400–950 nm was adopted, with a spectral resolution of 5 nm. Multispectral images of the reflective plate and 42 mineral samples in the 532 nm wavelength range were obtained, as shown in Figure 2. The spectral intensities of the target and reflective plate at corresponding pixel locations were extracted, and the target reflectance was derived using Equation (2). To ensure consistency between spectral measurements and subsequent underwater laser experiments, particular attention was given to the data acquisition design. Specifically, the mineral samples were obtained from an online store and have an irregular shape. Considering that when a multispectral camera captures targets located at different positions within its FOV, the surface non-uniformity of the targets may cause brightness differences between the center and edges of the image, resulting in changes in the spectral response. These targets were specifically selected to represent commercially valuable seabed mineral resources, such as manganese nodules and cobalt-rich crusts, as well as typical seabed rocks, covering a representative range of surface roughness and reflectivity found

in marine exploration scenarios. Six targets with relatively flat and large surfaces were selected to ensure the repeatability of the detection data, as shown in Figure 3. The same surface was subsequently used as the contact interface in the underwater laser experiments. To ensure the rigor of the experimental data, the spectral intensity at the central point of each mineral specimen was selected as I_{ore}, and in the underwater laser experiments, the laser beam was directed precisely to this central point. This experimental design provides a reliable reflection of both the performance of the SPL system constructed in this study and its feasibility for underwater detection applications.

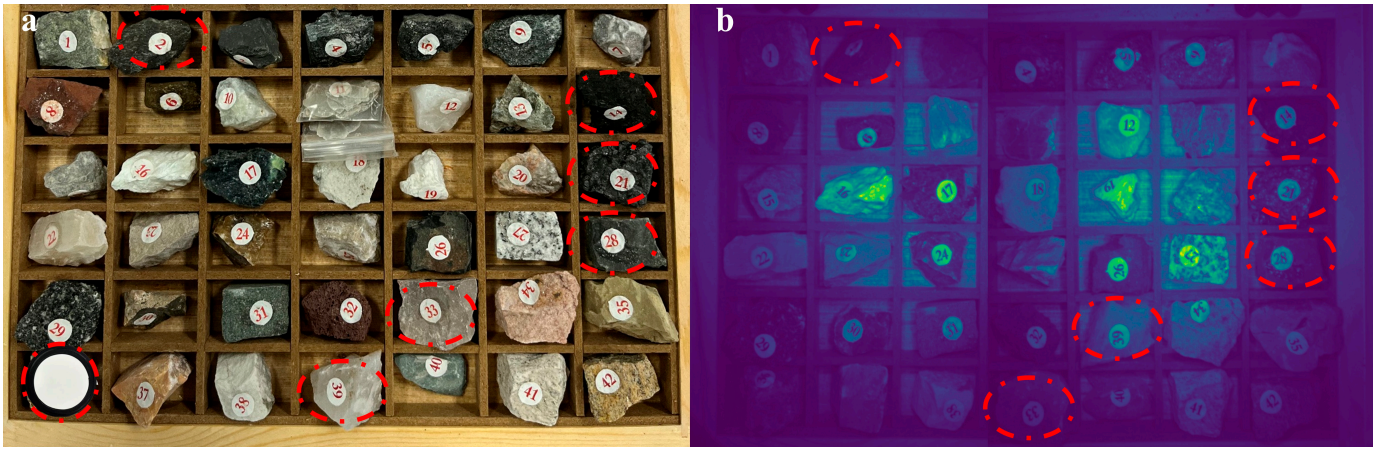

Figure 2. Spectral diagram of ore target: (**a**) Photograph of the mineral specimen tray; (**b**) spectral response of the specimen tray at 532 nm. The red ellipses indicate the targets selected for this study.

Figure 3. Selected seven targets with different reflectivity: Num.0: reflective plate (0.97); Num.2: manganese ore (0.23); Num.14: coal (0.25); Num.21: graphite (0.35); Num.28: basalt (0.29); Num.33: limestone (0.48); Num.39: quartzite (0.53).

2.4. Ranging Error Estimation

To evaluate ranging performance, peak detection was applied to extract time-of-flight (ToF) values. The peak signal refers to the electrical response generated when photons reach the target surface, undergo scattering, and are subsequently received by the detector, while the ToF corresponds to the interval between photon emission and detection. For each experimental condition, 30 measurements were acquired. The standard deviation (SD) of ToF was calculated as:

$$SD = \sqrt{\frac{\sum_{i=1}^{N} (t_i - \bar{t})^2}{N}} \quad (3)$$

where t_i is the ToF for the ith measurement, t is the mean ToF, and N is the number of samples. A smaller SD corresponds to higher measurement accuracy.

3. Experimental Setup

A modular experimental platform was constructed in a 4 m indoor water tank to investigate the influence of environmental and system parameters on underwater SPL performance. The reason for choosing 4 m as the water tank is that this is currently the only experimental condition available, and the theoretical model validation should be carried out first. Although the length of the water tank is 4 m, under high turbidity (C3 = 4.22 m^{-1}), this optical depth is sufficient to simulate the attenuation of transmitted signals in coastal environments. The size of the water tank is 4 m × 30 cm × 30 cm, with a glass thickness of 1 cm on the side wall. For different measurements, the water depth in the tank is 25 cm. The platform enables attenuation calibration, suppression of near-field interference, and simulation of complex aquatic conditions. The transmission loss of the tank window was calibrated by an optical power meter. Since the front glass wall was not a specially designed transmission window, its surface was relatively rough. When the laser beam was directly incident on it, the resulting Fresnel reflection generated intense background signals, which saturated the SPAD and masked the near-field echoes (distance < 0.5 m). Owing to the high sensitivity of the SPAD, even for a receiver with a narrow FOV, the reflected light from the tank's front wall could still lead to SPAD saturation. As shown in Figure 4, a nanosecond pulse passes through an energy-attenuation filter to prevent SPAD saturation and maintain a linear response. Adjusting the FOV would inevitably cause the loss of effective signals. To suppress such interference, two reflectors (R1, R2) were adopted to redirect the optical path, with the light propagating in the sequence of horizontal → vertical → horizontal before entering the water. The horizontal distance between R1 and the SPL system was fixed at 270 cm.

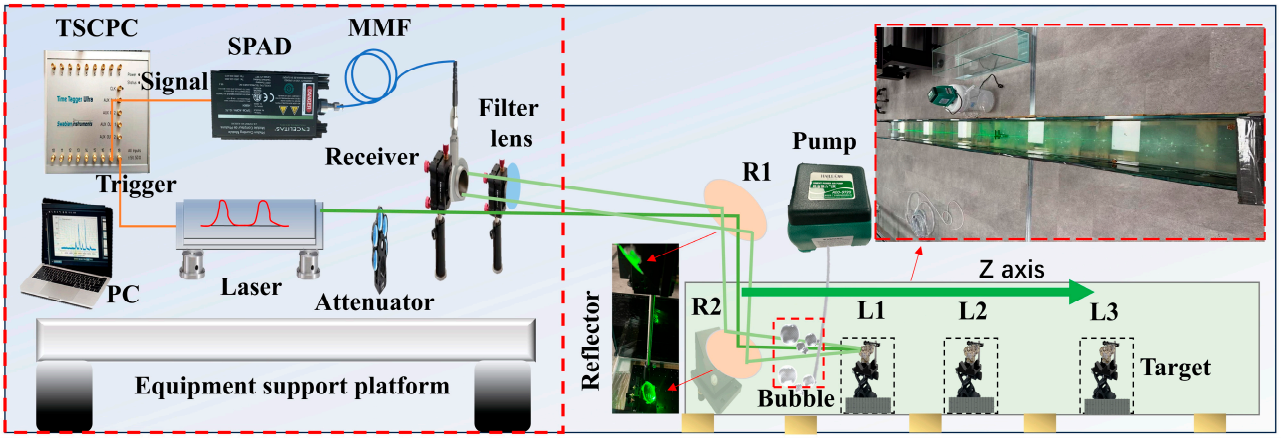

Figure 4. Experimental setup in a 4 m indoor water tank illustrating the beam path and the bubble diffuser. R1 and R2 refer to the reflectors, and L1, L2, and L3 refer to the target distances. The Z-axis direction is the direction of laser transmission.

Disturbances caused by oceanic turbulence and biological activity were simulated under controlled laboratory conditions. A 50 µm porous ceramic bubble diffuser, connected to an air pump, was positioned 20 cm below the water surface along the laser path to generate suspended bubbles, simulating specific scattering environments. However, it should be noted that this setup primarily focuses on the scattering and attenuation aspects of turbid water. It does not account for the refractive index fluctuations (optical scintillation) characteristic of complex oceanic turbulence driven by temperature and salinity gradients. The conditions represented here are more similar to coastal or estuarine zones with high concentrations of suspended inorganic particles. The full experimental configuration is shown in Figure 4.

A high-control multi-parameter optical attenuation experiment was conducted to investigate the coupling effects of turbidity, distance, integration time, and laser energy on system performance. A full-factorial design was adopted to manipulate five key variables. Four types of media were employed to represent different turbidity levels, as shown in Figure 5, including Air, Tapwater, Muddywater1 (simulated by mixing $NaHCO_3$ and potassium–magnesium compounds [26] in tap water), and Muddywater2 (prepared by further adding 5 mL of milk to Muddywater1 to enhance turbidity).

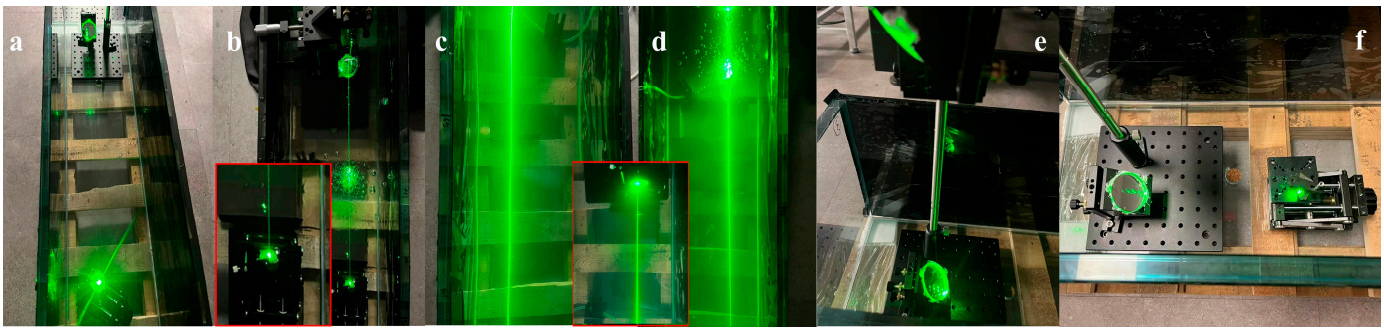

Figure 5. Water media conditions used: (**a**) Air; (**b**) Tapwater; (**c**) Muddywater1; (**d**) Muddywater2; (**e**) reflectors (R1, R2) side structure; (**f**) top view of reflectors (R1, R2). The illustration circled in red shows the laser beam spot profile and backscattering halo observed in the respective water conditions, illustrating the beam broadening effect caused by scattering.

The point to be mentioned here is that during the measurement of Muddywater1 and Muddywater2, it is necessary to continuously stir the bottom of the water tank to prevent the settling of dissolved substances. Seven target samples with distinct reflectance characteristics were selected, as shown in Figure 3, ranging from a reflective plate (0.97) to minerals such as beam geometry manganese ore (0.23), coal (0.25), graphite (0.35), basalt (0.29), limestone (0.48), and quartzite (0.53). The target distances measured from the center of the lower mirror to the target surface are L1, L2, and L3, as shown in Figure 4, which are set to 50 cm, 100 cm, and 200 cm, respectively. Laser energy was adjusted to four levels using optical attenuation plates, corresponding to 10%, 1%, 50%, and 100% transmission. In addition, three integration times of 100 ms, 500 ms, and 1000 ms were employed to evaluate their effects on signal repeatability and detection accuracy. All experimental variables are shown in Table 2; the combination of all variables resulted in $4 \times 7 \times 3 \times 4 \times 3 = 1008$ experimental cases. For each case under the air condition, six consecutive measurements were acquired, whereas for underwater conditions, thirty consecutive measurements were acquired for each case. The TCSPC module was set with a 25 ps bin width and 3000 bins, covering a 75 ns window sufficient to capture all returns. All data acquisition and bin configurations were controlled via Python (3.14.2) scripts. This design enabled a comprehensive dataset representing signal characteristics and laser attenuation laws under multifactor coupling conditions.

Table 2. System experimental parameters.

Parameter	Symbol	Value
Target	Num.0	Reflective plate
	Num.2	Manganese ore
	Num.14	Coal
	Num.21	Graphite
	Num.28	Basalt
	Num.33	Limestone
	Num.39	Quartzite

Table 2. *Cont.*

Parameter	Symbol	Value
Laser energy Configuration	Channel 1	10%
	Channel 2	1%
	Channel 3	50%
	Channel 4	100%
Integration Time	T1	100 ms
	T2	500 ms
	T3	1000 ms
Distance	L1	50 cm
	L2	100 cm
	L3	200 cm
Attenuation	C1	0.11 m^{-1}
	C2	0.98 m^{-1}
	C3	4.22 m^{-1}

4. Experiment Analysis

4.1. Measurement of Water Attenuation Coefficients

To accurately simulate laser transmission in underwater environments, the attenuation coefficients of underwater conditions were calibrated in a 4 m tank using the Beer–Lambert law:

$$P_b = P_f \cdot \exp(-c \cdot D) \tag{4}$$

where P_f is the laser power before entering the water, P_b is the power after transmission, c is the attenuation coefficient (m^{-1}), and D is the transmission path length. However, due to additional optical losses at the air–glass–water interfaces and through the mirror system, a transmission efficiency coefficient ξ was introduced [19]. The coefficient $\xi \approx 0.75$ was determined by measuring power at two reference points (positions 1 and 3 in Figure 6a) in the dry tank and was incorporated into the revised attenuation formula:

$$c = \frac{-\ln \frac{P_b}{P_f \cdot \xi}}{D} \tag{5}$$

To minimize stray light and multipath reflections, the tank was covered with black film, and all experiments were conducted in a dark room. Since the laser spot was smaller than the area of the power meter, we placed the center of the power meter on the laser path. The four tested media were: Air, Tapwater (C1 = 0.11 m^{-1}), Muddywater1 (C2 = 0.98 m^{-1}), and Muddywater2 (C3 = 4.22 m^{-1}). These measurement results provide accurate optical characterization of the media and support later analyses of signal decay behavior. Importantly, air was included as a non-underwater reference medium to provide a baseline for comparison with turbid water conditions. This design allows a straightforward assessment of how different liquid environments influence the response and performance of the SPL system.

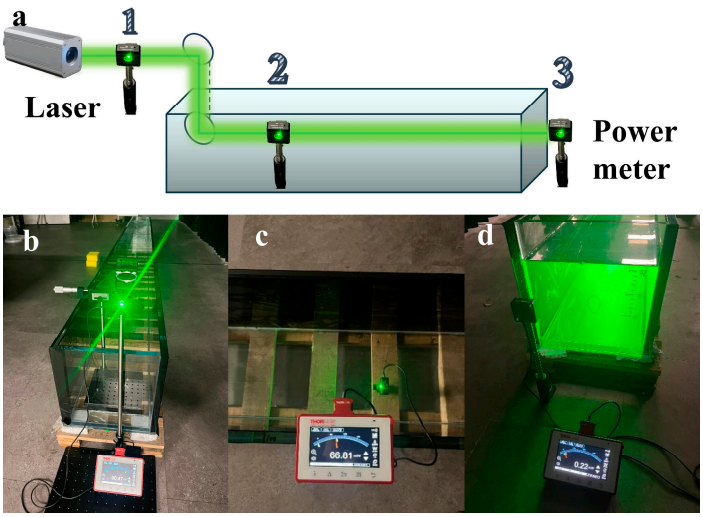

Figure 6. Measurement configuration for attenuation coefficient calibration: (**a**) measurement of the optical power meter at different positions in the water tank; (**b**) measurement at position 1; (**c**) measurement at position 2; (**d**) measurement at position 3.

4.2. Photon Histogram Signal Characteristics

The time-resolved histograms recorded by the TCSPC module characterize the echo signals under the specified parameter settings. A bin width of 25 ps provides extremely high temporal resolution, enabling the detection of subtle differences in echo signals. With 3000 bins, the total detection range corresponds to approximately 11 m, which fully covers all possible echo sources in the 4 m tank and prevents signal omission due to insufficient range. Unlike array detection, this study focuses on single-point detection, where small timing discrepancies inherent to the instrument remain. For instance, photon ToF measured with an oscilloscope can exhibit slight deviations compared to data from the SPL system. Therefore, system stability must be carefully considered.

The reflective plate was vertically placed on the laser path, and statistical analyses were conducted on the SPL signal reception under Channel 3 laser energy, different environmental media, and integration time, as shown in Figure 7. Each histogram plots ToF (x-axis) against photon counts (y-axis). Each subfigure corresponds to one of the four environmental media, and each contains three integration times: 100 ms (orange), 500 ms (green), and 1000 ms (purple). Three main peaks represent targets at 50, 100, and 200 cm, to better evaluate water transmission properties, and the attenuation length (AL), defined as the distance at which the power of the beam has decreased to 1/e of its original value, was introduced. It should be noted that AL presented here refers to one-way propagation, while the attenuation term in Equation (1) corresponds to the round-trip propagation of emission and return. There are three target placement distances for each attenuation.

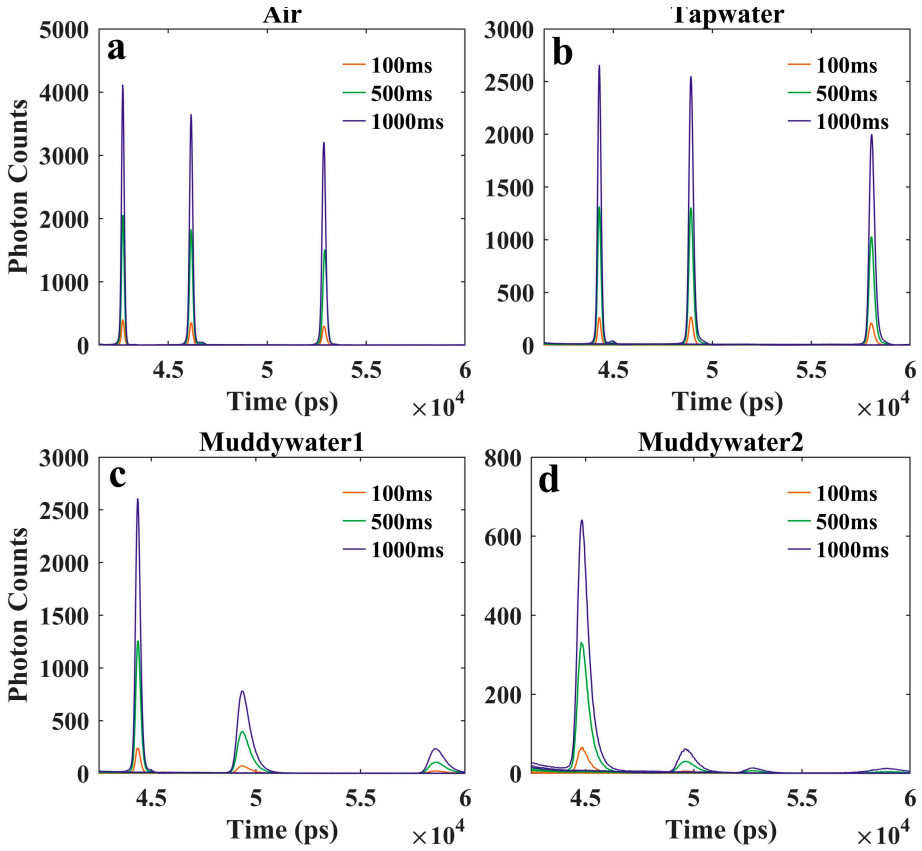

Figure 7. Photon count histograms for different environments and integration times under Channel 3: (**a**) Air; (**b**) Tapwater; (**c**) Muddywater1; (**d**) Muddywater2.

Figure 7a shows the echo signals in air, where the photon counts of the targets are relatively high. Figure 7b shows a low attenuation scenario where the laser energy attenuation can be negligible at three distances, and the target peak is clearly distinguishable with minimal background interference. In contrast, Figure 7d shows the detection signal under Muddywater2, where the laser energy is severely attenuated, making the target peaks almost indistinguishable. In such cases, near-field backscattering dominates the histograms, and applying range estimation to the entire histogram can lead to erroneous results due to strong backscatter peaks. Therefore, in the analysis, only the ToF data within a short window centered on the expected target range were processed. By default, this window was set to 1000 bins, as indicated by the horizontal axis range in Figure 7. It is noteworthy that photons travel at different velocities in air and water. As a result, the same target location produces distinct ToF values, as demonstrated in Figure 7.

The key results derived from Figure 7 can be summarized as follows:

(1) Turbidity effect: Signal strength decreases with increasing AL.
(2) Integration time effect: Longer integration significantly improves the SNR, especially in highly turbid conditions. For example, the 50 cm peak in Figure 7d increases from 60 counts (100 ms) to 600 counts (1000 ms).
(3) Backscattering interference: In highly turbid environments, near-field backscatter dominates and masks the true target return.

Figure 8 compares the photon counts for seven targets under four environmental conditions in Channel 3 with an integration time of 1000 ms. This figure intuitively quantifies the coupled influence of medium turbidity and target reflectivity on the SPL. Due to the differences in target reflectivity, significant discrepancies in photon counts are observed at the same distance. The reflective plate consistently shows the highest peak

counts across all media. For example, in air, its peak count is 1.3 times that of the second-highest (Quartz, Num.39). Even under Mddywater2 in Figure 8d, it still maintains a peak count of 600, which is 12 times higher than the weakest target (Coal, Num.14, 50 counts).

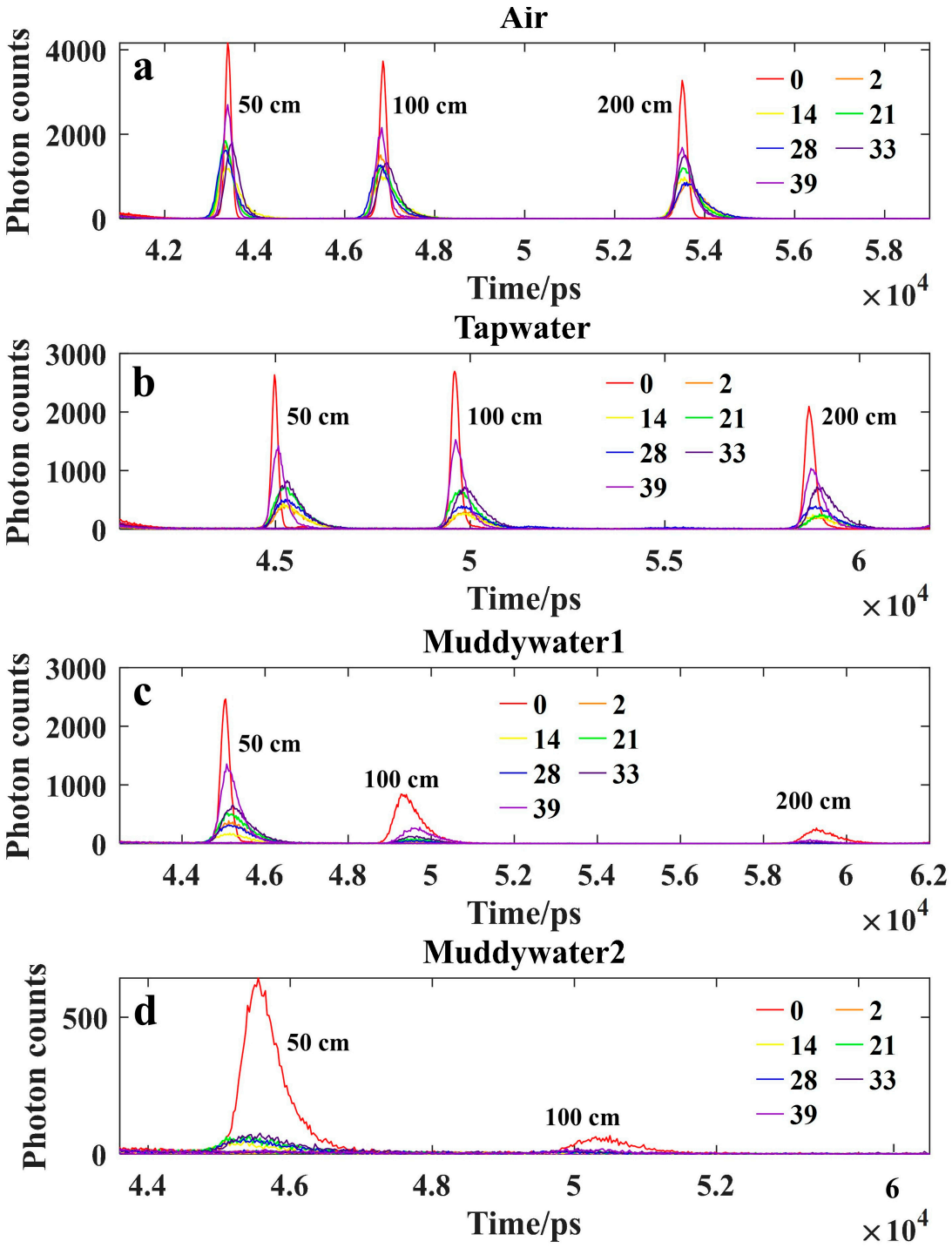

Figure 8. Photon-count peaks from seven targets at 1000 ms and 50% energy across four turbidities: (**a**) Air; (**b**) Tapwater; (**c**) Muddywater1; (**d**) Muddywater2.

Low-reflectivity targets, such as Manganese Num.2 and Coal Num.14, exhibit low peak counts even in air. Their peaks drop below 500 counts in Figure 8c and become almost indistinguishable in Figure 8d. This indicates that low-reflectivity targets are more sensitive to turbidity, exhibiting a much higher signal attenuation rate than high-reflectivity targets. These results confirm that turbidity is the dominant factor in signal attenuation, while

target reflectance primarily governs signal amplitude. Additionally, it was found that under Muddywater2, as shown in Figure 8d, when the target is at 100 cm, only the reflector has observable signal peaks, and when the target is at 200 cm, the signal of the target is almost undetectable. This provides some insights into the relationship between turbidity and detection distance.

It is worth mentioning that when processing the data in Figure 8, we discovered the phenomenon of forward shift in photon flight time, detected by high-reflectivity targets, which is physically attributed to strong multiple scattering and high reflectivity. When the photon flux is high for the high-reflectivity target, the probability of detecting photons at the early rising edge of the laser pulse increases, causing the statistical center of the recorded histogram to shift towards a shorter time.

4.3. Statistical Distribution and Bubble Influence

Figure 9 shows the statistical distribution of target peak position measurements and echo photon counts under different distances, turbidity, and bubble conditions. The horizontal axis indicates the target number, and the different colors in each column of each subgraph represent the peak signal comparison of the target at three measurement positions under different attenuation coefficients. Measurement accuracy declines with increasing distance: from 50 cm to 200 cm, the dispersion of measured positions broadens substantially. At the same distance, higher turbidity further increases dispersion due to enhanced particle scattering.

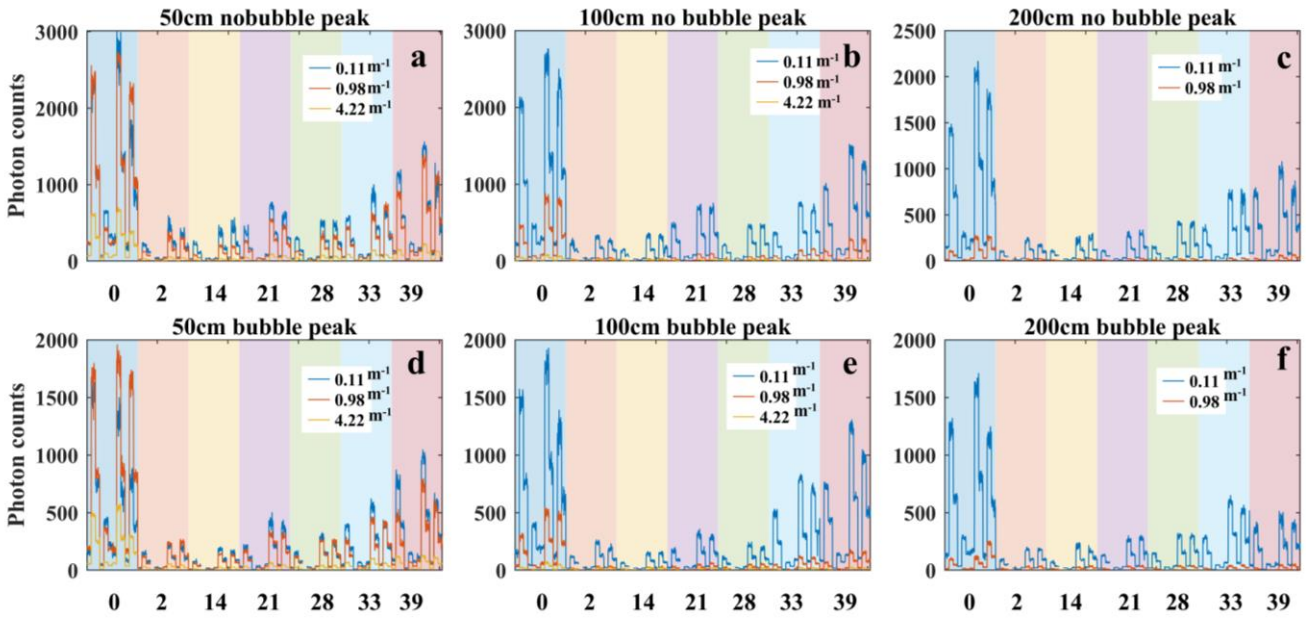

Figure 9. Photon-count statistics under varying distances, turbidity levels, and bubble conditions: (**a**–**c**) without bubbles at 50 cm, 100 cm, and 200 cm, respectively; (**d**–**f**) with bubbles at 50 cm, 100 cm, and 200 cm.

Bubbles introduce additional degradation. At long distances in highly attenuation water, valid measurement points diminish even at moderate reflectivity (0.48–0.53), indicating bubble-induced weakening of target echoes. At short distances, bubbles amplify jitter when reflectivity drops to 0.23–0.35. Reflectivity itself strongly affects accuracy: high-reflectivity targets yield concentrated distributions, whereas low-reflectivity ones are more dispersed.

The peak photon counts of target echoes are markedly attenuated under multifactor coupling, with turbidity identified as the dominant driver of signal degradation. In highly turbid water, suspended particles strongly enhance laser energy attenuation; for instance,

in Figure 9a, the peak photon count under condition C3 decreases by nearly 80% compared to C1. At short distances and under low attenuation, the trend of photon counts varies consistently with target reflectivity intensity (0.97–0.23), as shown in Figure 9. At 100 cm and C2 attenuation, distributions remain separable even at low reflectivity, but at 200 cm, only signals from 0.97 reflectivity targets remain detectable, while weaker reflections fall below the extraction threshold. Compared with the bubble-free condition, the presence of bubbles further reduced the peak counts by approximately 30%, highlighting their pronounced attenuating effect. Quantitative analysis of the peak variations provides a basis for intensity compensation in post-processing, and also indicates that calibrating the SPL system under high-turbidity, bubble-rich conditions enables reliable outdoor underwater detection.

4.4. Ranging Error Analysis

The system's ranging repeatability was evaluated through 30 repeated acquisition trials for each parameter combination. In this study, repeatability refers to the consistency of ranging results obtained from repeated measurements under identical experimental conditions and does not imply long-term system stability in varying environmental conditions. Each trial utilized a specific integration time, quantified by the SD of the peak ToF position across these trials. It should be noted that under high turbidity and low laser energy conditions, the photon arrival statistics deviate from Gaussian behavior, as evidenced by skewness and outliers in the boxplots. Therefore, the standard deviation is used here as a relative indicator of ranging repeatability for large-scale comparison rather than a complete error analysis.

We next evaluate the repeatability of the SPL system. Figures 10 and 11 present boxplot statistics of distance measurements under bubble-free conditions using 50% and 1% laser energy, respectively, for seven targets at 50 cm and 100 cm. Each dataset includes three integration times and three turbidity levels. The peak signal denotes the SPAD response to returned photons. By analyzing the positional trends of the peaks and the degree of dispersion, the results reveal how laser energy and multifactor coupling influence SPL ranging performance and demonstrate the system's high-ranging accuracy and repeatability.

In Figure 10, the six subplots' results show that increasing turbidity markedly degrades ranging accuracy, as evidenced by the widening boxplots and higher SD. Data distributions also become increasingly skewed. For example, in Figure 10E(d), the SD under C3 turbidity is 189% higher than C1, yet the system still maintains SD < 0.1092 ns under C3–100 cm–500 ms, verifying strong attenuation resistance. Extending the integration time can effectively improve the stability. Under the same conditions, the box width and the SD of 1000 ms integration are significantly reduced compared with 100 ms (Figure 10B,F), as more target photons can be accumulated for a longer period of time to improve the SNR. Distance and reflectivity are also coupled; an increasing distance exacerbates the decline in accuracy. As shown in Table 3, the SD at 100 cm is 60% higher than at 50 cm. The box width for high-reflectivity targets is significantly narrower than for low-reflectivity targets, with an SD difference of five times, highlighting the critical role of reflectivity in echo intensity and accuracy.

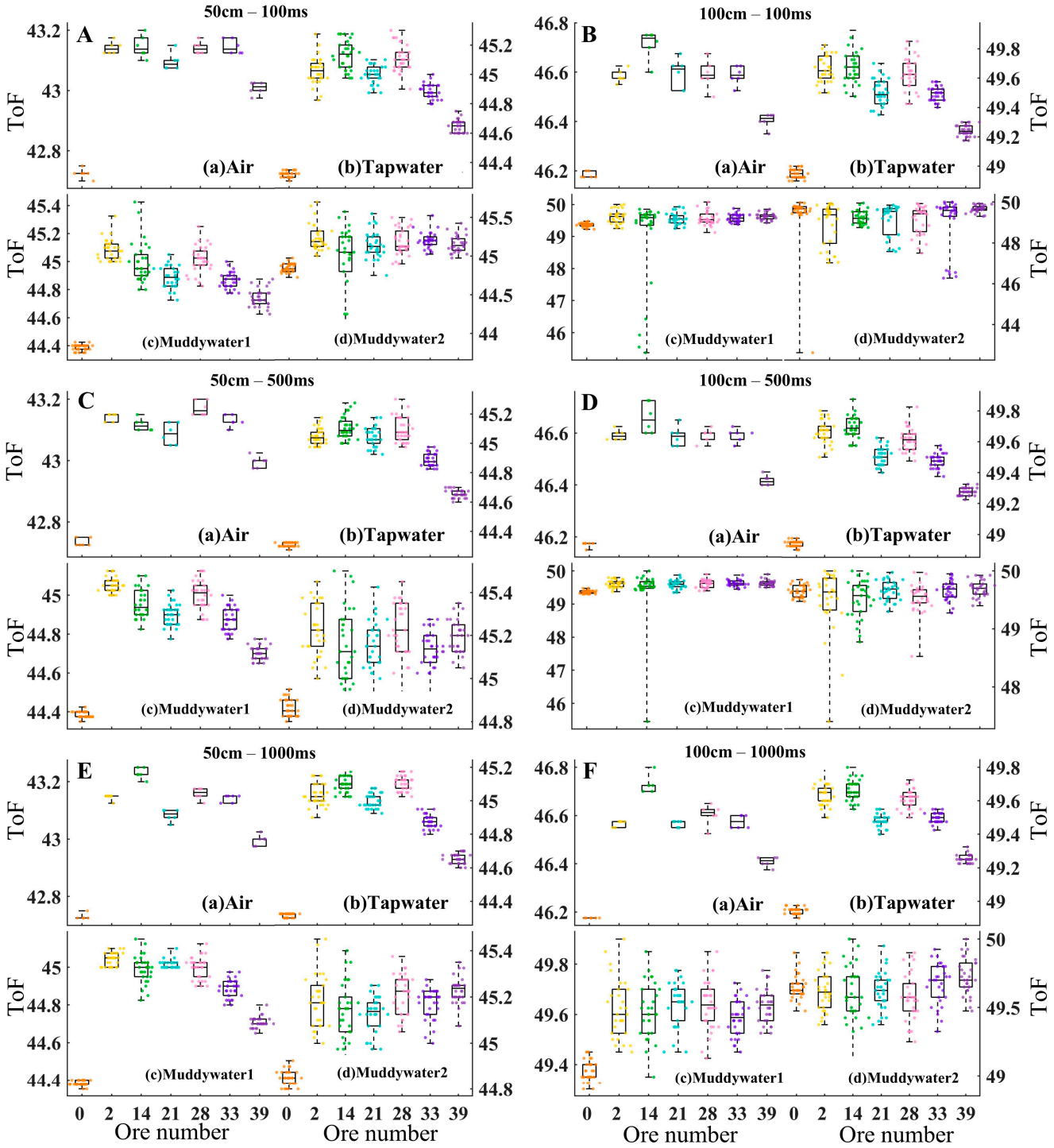

Figure 10. Boxplot statistics of ToF, which represents the interval from photon emission to detection at 50 cm and 100 cm in four environments under Channel 3: (**A**) 50 cm–100 ms; (**B**) 100 cm–100 ms; (**C**) 50 cm–500 ms; (**D**) 100 cm–500 ms; (**E**) 50 cm–1000 ms; (**F**) 100 cm–1000 ms. (**a**–**d**) represent Air, Tapwater, Muddywater1, and Muddywater2.

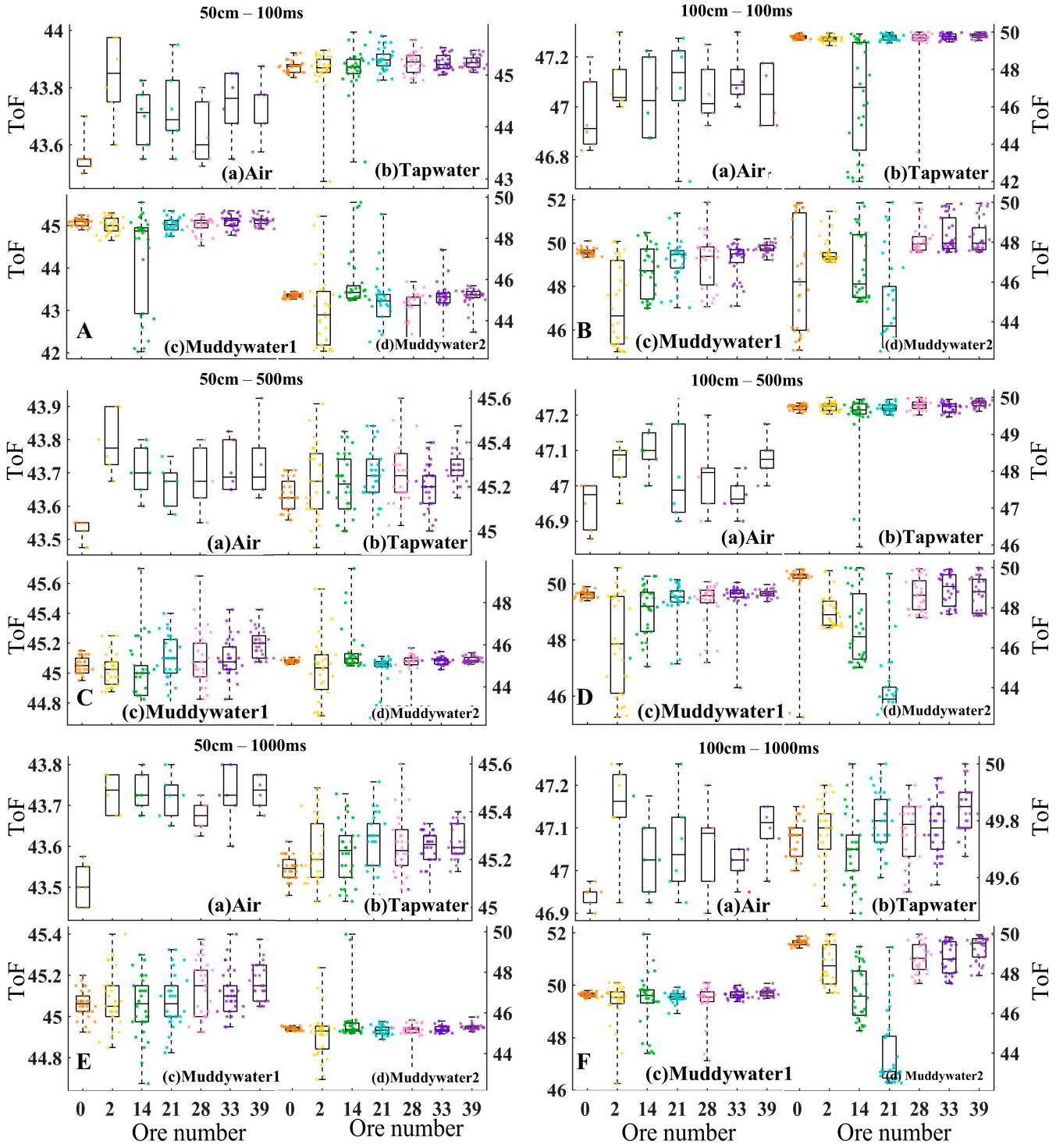

Figure 11. Statistics of photon ToF, which represents the interval from photon emission to detection at 50 cm and 100 cm in four environments under Channel 2: (**A**) 50 cm–100 ms; (**B**) 100 cm–100 ms; (**C**) 50 cm–500 ms; (**D**) 100 cm–500 ms; (**E**) 50 cm–1000 ms; (**F**) 100 cm–1000 ms. (**a**–**d**) represent Air, Tapwater, Muddywater1, and Muddywater2.

Table 3. Mean and SD of photon ToF for num0 under the multi-parameter attenuation coupling model.

Laser Energy	Time	Distance	C1	C2	C3
Channel 1	100 ms	50 cm	44.72 ± 0.041 ns	44.70 ± 0.039 ns	45.16 ± 0.094 ns
		100 cm	49.31 ± 0.052 ns	49.57 ± 0.090 ns	49.63 ± 0.185 ns
	500 ms	50 cm	44.72 ± 0.028 ns	44.66 ± 0.041 ns	45.12 ± 0.057 ns
		100 cm	49.28 ± 0.033 ns	49.61 ± 0.068 ns	49.68 ± 0.119 ns
	1000 ms	50 cm	44.71 ± 0.021 ns	44.66 ± 0.025 ns	45.15 ± 0.048 ns
		100 cm	49.28 ± 0.028 ns	49.60 ± 0.060 ns	49.67 ± 0.109 ns
Channel 2	100 ms	50 cm	45.15 ± 0.114 ns	45.09 ± 0.087 ns	45.22 ± 0.106 ns
		100 cm	49.74 ± 0.101 ns	49.60 ± 0.167 ns	46.30 ± 2.701 ns
	500 ms	50 cm	45.16 ± 0.070 ns	45.05 ± 0.056 ns	45.22 ± 0.085 ns
		100 cm	49.74 ± 0.067 ns	49.62 ± 0.124 ns	49.16 ± 1.785 ns
	1000 ms	50 cm	45.16 ± 0.049 ns	45.06 ± 0.065 ns	45.23 ± 0.087 ns
		100 cm	49.73 ± 0.062 ns	49.64 ± 0.077 ns	49.56 ± 0.148 ns
Channel 3	100 ms	50 cm	44.32 ± 0.020 ns	44.39 ± 0.021 ns	44.85 ± 0.056 ns
		100 cm	48.95 ± 0.031 ns	49.36 ± 0.059 ns	49.41 ± 1.291 ns
	500 ms	50 cm	44.31 ± 0.014 ns	44.39 ± 0.015 ns	44.86 ± 0.040 ns
		100 cm	48.94 ± 0.019 ns	49.36 ± 0.046 ns	49.65 ± 0.102 ns
	1000 ms	50 cm	44.32 ± 0.011 ns	44.38 ± 0.014 ns	44.85 ± 0.033 ns
		100 cm	48.94 ± 0.018 ns	49.37 ± 0.040 ns	49.65 ± 0.087 ns
Channel 4	100 ms	50 cm	44.14 ± 0.015 ns	44.23 ± 0.025 ns	44.72 ± 0.058 ns
		100 cm	48.80 ± 0.031 ns	49.23 ± 0.051 ns	49.57 ± 0.135 ns
	500 ms	50 cm	44.14 ± 0.012 ns	44.21 ± 0.019 ns	44.71 ± 0.029 ns
		100 cm	48.79 ± 0.014 ns	49.21 ± 0.034 ns	49.63 ± 0.151 ns
	1000 ms	50 cm	44.15 ± 0.008 ns	44.23 ± 0.010 ns	44.71 ± 0.025 ns
		100 cm	48.80 ± 0.010 ns	49.22 ± 0.028 ns	49.63 ± 0.101 ns

The core difference between Figures 10 and 11 lies in the significant degradation of ranging accuracy caused by low laser energy, as evidenced by the generally increased width of the box and the SD that is three times that under 50% energy. For instance, as shown in Table 3, under the condition of C1 −50 cm–1000 ms, the SD increases from 0.0117 ns to 0.0490 ns, which is attributed to insufficient SNR resulting from a sharp reduction in the number of echo photons from the target. Additionally, under the same conditions, the skewness of the peak distribution becomes more stable with increasing integration time. Although extending the integration time can partially mitigate the decline in accuracy, for example, the SD at 1000 ms is reduced by 57% compared to 100 ms, as shown in Table 3, it still does not reach the performance level of Channel 3. It is worth noting that the response pattern of reflectance remains consistent, and high-reflectance targets can still maintain relatively good accuracy.

Table 3 shows the mean and SD of the ToF measured for num0 under the multi-parameter attenuation coupling model. It can be concluded that as turbidity increases from C1 to C3, the SD of ToF under Channel 3–50 cm–1000 ms rises from 0.0117 ns to 0.0338 ns. Even at high turbidity levels, the SD at 100 cm remains within 0.1092 ns, indicating that the system has strong attenuation resistance. A comparison of the SD values in Table 3 indicates that Channel 3 is currently the optimal energy choice. For example, at C1–50 cm−1000 ms, Channel 3 has an SD of 0.0117 ns, slightly higher than Channel 4's SD (0.0080 ns). Under Channel 4, the SPAD enters a saturation regime where the high density of backscattered photons triggers the 'dead time' effect. During this period, the detector is unresponsive to subsequent photon events, leading to a distortion of the echo-pulse shape and a shift in the perceived peak position. In comparison, Channel 3 avoids saturation issues while balancing

SNR and maintaining accuracy comparable to Channel 4. Channel 2 performs the worst: under C1 −50 cm–1000 ms, its SD is 0.0490 ns, four times that of Channel 3, indicating that signal loss at low energies leads to a significant increase in errors. To mitigate this in future iterations, we propose the implementation of an active quenching circuit with adjustable dead time or the application of a mathematical correction model based on the incident photon flux to restore the true signal dynamics.

Overall, higher turbidity increases SD, whereas longer integration times improve ranging precision. Under the parameter settings of this study, Channel 3 was identified as the optimal energy configuration, providing a balance between strong return signals and minimal SPAD saturation risk; this conclusion can also be demonstrated in the next section on reflectivity inversion. Due to photon losses during dead time, the total integrated photon count is lower than the actual arrival rate, leading to a systematic underestimation of the inverted reflectance. We explicitly state that this effect is more pronounced for Channel 4 compared to Channel 3, which is a key reason why Channel 3 often represents a more optimal operating, balancing signal level against saturation and pile-up distortions. In contrast, Channel 4 suffers from dead time caused by saturation, while Channel 2 exhibits poor SNR. The SD of high-reflectivity targets was also significantly lower than that of low-reflectivity targets. These results indicate that the impact of laser energy and integration time on ranging stability is strongly dependent on turbidity. Under high turbidity conditions, increasing laser energy does not yield proportional improvement in ranging precision, demonstrating a clear non-additive interaction between system parameters. Under the optimal settings (Channel 3–1000 ms), the system achieved an SD of 0.0117 ns at 50 cm–C1 and 0.0877 ns at 100 cm–C3, demonstrating strong ranging repeatability and revealing the problems encountered in underwater detection.

In addition, a comparative analysis between Channel 3 and Channel 4 energy configurations was conducted to quantitatively evaluate the impact of pile-up effects on ranging accuracy. Based on the comparison of the mean and standard deviation of photon time-of-flight (ToF) measurements for the high-reflectivity target (num0) reported in Table 3, it is observed that, regardless of water quality, the photon ToF obtained under Channel 4 is consistently shorter than that under Channel 3 when the integration time and target distance are identical. This behavior corresponds to the forward temporal shift discussed above. These observations suggest that excessively high-laser pulse energy may lead to an underestimation of the true target distance, providing valuable practical insight for subsequent underwater LiDAR studies. Furthermore, it is also observed that, under identical integration time and target distance conditions, the standard deviation under Channel 4 is generally smaller than that under Channel 3 across different water qualities, indicating that the reflected signal becomes more dominant at higher energy levels, resulting in reduced timing jitter.

4.5. System Reflectance Inversion

In Figure 12, the boxes and points in different colors represent the reflectivity distribution of different targets. The median of each boxplot indicates the central tendency of reflectivity, while a more concentrated point distribution corresponds to better measurement stability. Under the same distance and integration time, the turbidity has a significant effect on the inversion accuracy, from a to d, and the overall trend of the interquartile range (IQR) of the box plot is increasing. In addition, in Figure 12E(a), the mean reflectivity of Quartz Num.39 is 0.45 with an IQR of 0.03, while in Figure 12E(d), its mean reflectivity is 0.35 with an IQR of 0.08. This is due to the severe scattering of photons in the C2 environment with added milk. Consequently, the SNR drops sharply, leading to increased errors.

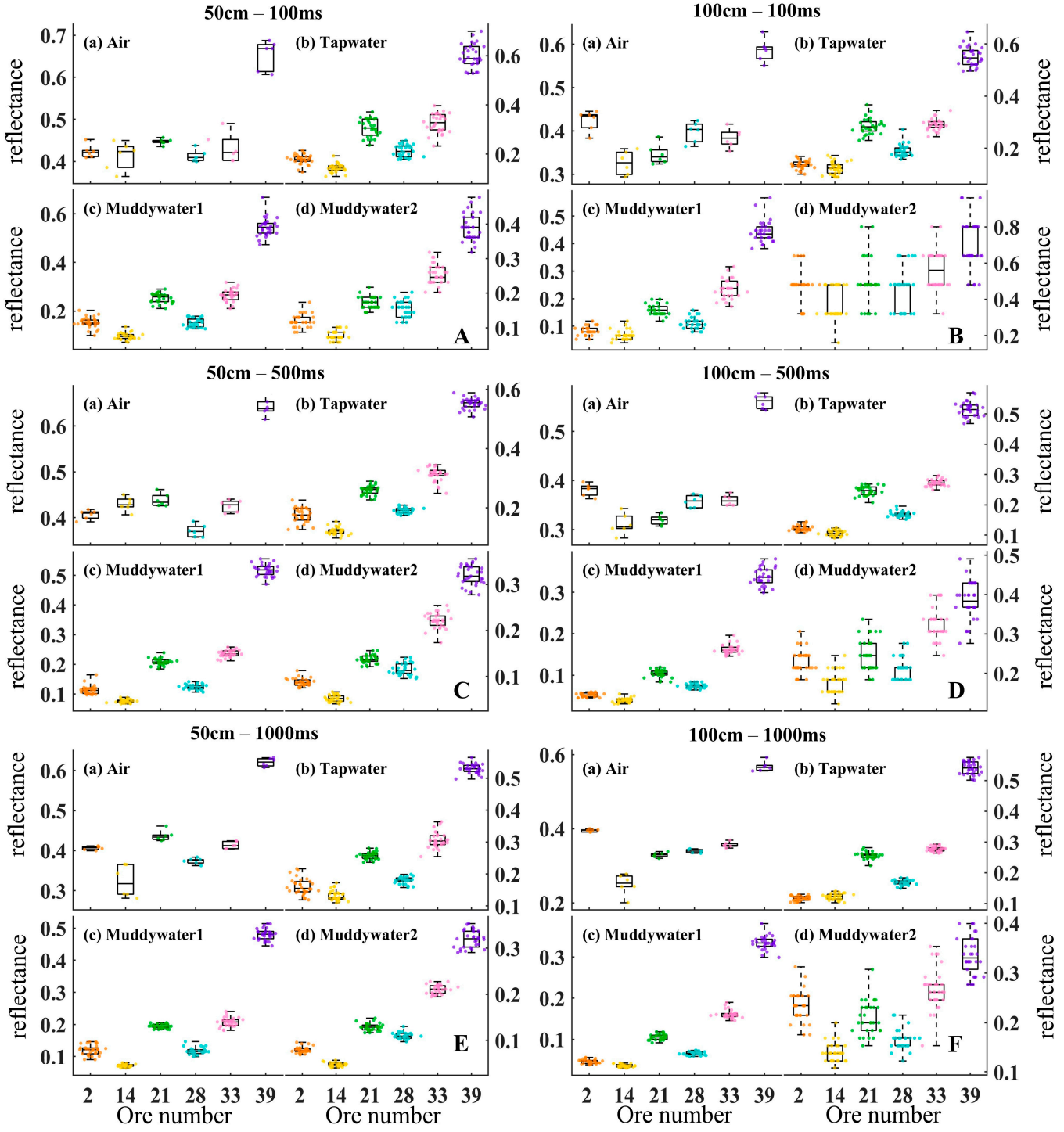

Figure 12. Statistical measurements of target reflectance at different turbidity levels, distances, and integration times: (**A**) 50 cm−100 ms; (**B**) 100 cm−100 ms; (**C**) 50 cm−500 ms; (**D**) 100 cm−500 ms; (**E**) 50 cm−1000 ms; (**F**) 100 cm−1000 ms. (**a**) Air, (**b**) Tapwater, (**c**) Muddywater1, and (**d**) Muddywater2.

The effect of distance is relatively weak: from 50 cm to 100 cm at the same integration time and turbidity, the IQR increases slightly, and the inversion error rises slightly. For example, the IQR of limestone Num.33 in Figure 12E is 0.02, and the IQR of the same target in Figure 12F is 0.04, which comes from the fact that the distance increase makes the laser transmission path lengthened, the doubling of the AL intensifies the energy attenuation, the target echoes are weakened, and the target reflectivity is negatively correlated with the inversion error. The box plot IQR of the target with high reflectivity is smaller, for example,

the IQR of Num.39 quartzite is 0.02, and the IQR of Num.14 coal is 0.04 in Figure 12E. Highly reflectance targets produce stronger echoes, a higher SNR, and smaller inversion errors. For low-reflectivity targets, fewer photons return after multiple scatterings, resulting in larger reflection inversion errors.

However, it should be noted that the inversion model used in this study is Lambert scattering, assuming the targets are a standard Lambertian body. However, natural minerals exhibit complex Bidirectional Reflectance Distribution Function (BRDF) underwater, and the surface roughness and angular scattering characteristics of minerals result in observed discreteness, especially for low-reflectivity targets. Therefore, under specific monostable geometric conditions of the SPL system, the values should be interpreted as "effective reflectance".

Figure 12 provides critical support for the core conclusions of this paper: under conditions of low turbidity, short distance, and long integration time, the reflectivity inversion error of high-reflectivity targets is less than 3%. For example, in Figure 12E(b), the mean reflectivity of Num.39 is 0.529, which differs from the calibrated value of the spectral camera by only 0.01; under the conditions of 100 cm and 1000 ms, the measured mean reflectivity is 0.54, with a deviation of 0.1 from the spectral camera's calibrated value. In contrast, low-reflectivity targets do not achieve such high inversion accuracy. For instance, in Figure 12E(b), the mean reflectivity of Num.21 is 0.257, and the error between this value and the calibrated value of the spectral camera reaches 20%. It should be particularly emphasized that the reflectivity values of ores in this study are referenced to the calibration results of the spectral camera, and this process is accomplished based on the selection of pixel points.

As the experimental results suggest, the turbidity is the dominant factor causing laser attenuation, integration time serves as an optimization means, and distance exerts a relatively minor influence. Furthermore, these results provide a basis for parameter optimization. Employing a long integration time combined with moderate laser energy yields a favorable detection performance. For low-reflectivity targets, the inversion accuracy can be improved by extending the integration time or increasing the laser energy.

In Section 4, data under each experimental condition were obtained from 30 consecutive measurements. In addition, for each individual scenario, the data processing procedure adopts the averaged signal derived from these 30 repeated measurements, as illustrated in Figures 7 and 8. Consequently, uncertainty propagation and reproducibility arising from multiple data realizations within the same experimental scenario are inherently accounted for. For example, uncertainty propagation observed during data processing includes the following:

(1) Attenuation coefficient (c): Uncertainty stems from power meter precision (±2%) and path length measurement (±0.5 cm), already considered in the calibrated $c = 0.11 \pm 0.01\ m^{-1}$ (Tapwater) to $4.22 \pm 0.05\ m^{-1}$ (Muddywater2).
(2) Reflectance inversion: Uncertainty includes photon-count noise and multispectral calibration error, clarified as ±0.02–0.04 for all targets.
(3) Ranging SD: Uncertainty from TCSPC time-base stability and environmental vibration, noted as ±0.002–0.005 ns.

5. Conclusions

To address the challenge of achieving high-precision underwater detection under strong attenuation and scattering, we, for the first time, conducted a comprehensive evaluation of the signal characteristics of the SPL system under multifactor coupling. The study was carried out as a full-factorial experiment in a 4 m water tank. The findings of this study demonstrate high-ranging repeatability and strong anti-attenuation capability, with the SPL system achieving sub-nanosecond ranging repeatability. For example, the clear influence of system and environmental parameters includes the following: Turbidity was a dominant

factor that drove signal attenuation, while target reflectivity governed echo intensity and ranging accuracy. Furthermore, the integration time significantly improved the SNR in high-attenuation conditions, whereas excessive laser energy risked SPAD saturation; therefore, laser energy should be carefully balanced between ensuring sufficient signal strength and maintaining stable detection performance. Regarding high-ranging repeatability and anti-attenuation capability, The SPL system achieved sub-nanosecond ranging repeatability. For C1, the SD increased from 0.0117 ns at 50 cm to 0.0187 ns at 100 cm, whereas for C3, it increased slightly, from 0.0338 ns to 0.0877 ns over the same depth range. Furthermore, regarding accurate reflectance inversion with clear trends, for high-reflectivity minerals, inversion errors were below 3% when validated against multispectral calibration, while errors increased exponentially with turbidity and were higher for low-reflectivity targets. Regarding comprehensive analysis and dataset contribution, this work provides a holistic analysis of SPL signal dynamics under realistic underwater interference and validates reflectance inversion using multispectral imaging. The resulting 111-band reflectance dataset lays a foundation for future underwater spectral libraries and classification algorithms. The conclusions obtained are of broad applicability, thereby advancing the development of underwater LiDAR technology.

While the 4 m experimental tank allows for high-precision control of multi-parameter coupling, it is important to acknowledge its limitations in replicating the full complexity of oceanic environments. It should be emphasized that the experimental validation in this study is limited to a maximum ranging distance of 200 cm in a controlled laboratory tank. Broader applicability is discussed, primarily in terms of optical attenuation length rather than direct physical distance extrapolation to open-water environments. Real-world conditions involved spatial–temporal variability in currents and significant ambient light noise at varying depths. Our results represent the system's intrinsic response under specific attenuation levels without external solar interference, serving as a foundational baseline for predicting performance in deep-sea or nighttime operations where ambient noise is minimized.

Future research will focus on extending this work in several directions. First, the SPL system will be integrated onto an autonomous underwater vehicle (AUV), and the detection model and methodology proposed in this study will be tested in real marine environments. These experiments aim to verify the feasibility of the proposed detection framework in open-water conditions and to evaluate its long-term stability and performance under dynamic scattering, ambient light interference, and varying flow conditions. Based on the experimental outcomes, the proposed theoretical framework will be further refined and optimized. Second, the developed methodology will be integrated into a multispectral SPL platform to enable fine-grained spectral discrimination of underwater minerals. Finally, advanced signal processing algorithms will be explored to enhance SNR, suppress background noise, and further improve reflectance inversion accuracy. These efforts will broaden the applicability of SPL systems for marine resource exploration, environmental monitoring, and underwater target recognition.

Author Contributions: Conceptualization, C.W. and S.Z.; methodology, C.W.; software, S.Z.; investigation, C.H. and W.Y.; writing—review and editing, Y.C. and J.W.; project administration, Y.C. and C.L.; funding acquisition, S.L. All authors have read and agreed to the published version of the manuscript.

Funding: This research was funded by the Zhejiang Provincial "Jianbing Lingyan" Research and Development Program of China (2025C02039, 2024C03032, 2024C01126, and 2023C03012); the Research Funds of Hangzhou Institute for Advanced Study, University of Chinese Academy of Science (B02006C021026, B02006C021022); the China Postdoctoral Science Foundation (2025M780773); the Natural Science Foundation of Zhejiang province (QN26F030002); and the matching funds of Hangzhou Institute for Advanced Study, UCAS for the Zhejiang Provincial "Jianbing Lingyan" Research and Development Program of China (B02006C021029).

Data Availability Statement: The data presented in this study are available upon request from the corresponding author. The data are not publicly available due to third party agreements. Data were obtained from Lidar Laboratory of Hangzhou Institute for Advanced Study, University of Chinese Academy of Sciences.

Conflicts of Interest: The authors declare no conflicts of interest.

Abbreviations

The following abbreviations are used in this manuscript:

SD	standard deviation
SPL	Single-photon LiDAR
SPAD	Single-photon avalanche diode
FOV	Field of view
TOF	Time to flight
MMF	Multimode fiber
IQR	Interquartile range
SNR	Signal-to-noise ratio
TCSPC	Time-correlated single-photon counting
AUV	Autonomous underwater vehicle
BRDF	Bidirectional Reflectance Distribution Function

References

1. Shangguan, M.; Yang, Z.; Lin, Z.; Liao, Z.; Guo, Y.; Liu, C. Remote sensing oil in water with an all-fiber underwater single-photon Raman lidar. *Appl. Opt.* **2023**, *62*, 5301–5305. [CrossRef] [PubMed]
2. Shangguan, M.; Weng, Z.; Lin, Z.; Lee, Z.; Yang, Z.; Sun, J.; Wu, T.; Zhang, Y.; Wen, C. Day and night continuous high-resolution shallow-water depth detection with single-photon underwater lidar. *Opt. Express* **2023**, *31*, 43950–43962. [CrossRef]
3. Hoque, S.; Abdullah, M.A.; Alayed, M.; Elamien, M.; Deen, M.J. Silicon-Based Single Photon Avalanche Diode Technologies: Structures, Performance, and Challenges. *IEEE Electron Devices Rev.* **2025**, *2*, 69–97. [CrossRef]
4. Durini, D.; Paschen, U.; Schwinger, A.; Spickermann, A. 11-Silicon based single-photon avalanche diode (SPAD) technology for low-light and high-speed applications. *Photodetectors* **2016**, 345–371. [CrossRef]
5. Deng, Y.; Liu, J.; Xiao, H.; Shu, S.; Wang, S.; Zhang, B. Developments in Atmospheric Remote Sensing Lidar Based on Single-Photon Detection. *Laser Optoelectron. Prog.* **2025**, *62*, 1000002. [CrossRef]
6. Churnside, J.H.; Shaw, J.A. Lidar remote sensing of the aquatic environment: Invited. *Appl. Opt.* **2020**, *59*, C92–C99. [CrossRef]
7. Pashayev, A.M.; Allahverdiyev, K.R.; Tagiyev, B.G.; Sadikhov, I.Z. Light induced fluorescence LIDAR developed and employed at the National Aviation Academy of Azerbaijan. In *19th International Conference and School on Quantum Electronics: Laser Physics and Applications*; SPIE: Bellingham, WA, USA, 2017; Volume 10226, p. 102260W. [CrossRef]
8. Shangguan, M.; Xia, H.; Wang, C.; Qiu, J.; Shentu, G.; Zhang, Q.; Dou, X.; Pan, J.-W. All-fiber upconversion high spectral resolution wind lidar using a Fabry-Perot interferometer. *Opt. Express* **2016**, *24*, 19322–19336. [CrossRef]
9. Shangguan, M.; Xia, H.; Wang, C.; Qiu, J.; Lin, S.; Dou, X.; Zhang, Q.; Pan, J.-W. Dual-frequency Doppler lidar for wind detection with a superconducting nanowire single-photon detector. *Opt. Lett.* **2017**, *42*, 3541–3544. [CrossRef]
10. Yu, C.; Shangguan, M.; Xia, H.; Zhang, J.; Dou, X.; Pan, J.W. Fully integrated free-running InGaAs/InP single-photon detector for accurate lidar applications. *Opt. Express* **2017**, *25*, 14611–14620. [CrossRef]
11. Bai, J.; Gao, S.; Niu, Z.; Zhang, C.; Bi, K.; Sun, G.; Huang, Y. A Novel Algorithm for Leaf Incidence Angle Effect Correction of Hyperspectral LiDAR. *IEEE Trans. Geosci. Remote Sens.* **2021**, *60*, 1–9. [CrossRef]
12. Xia, H.; Shangguan, M.; Shentu, G.; Wang, C.; Qiu, J.; Zheng, M.; Xie, X.; Dou, X.; Zhang, Q.; Pan, J.-W. Brillouin optical time-domain reflectometry using up-conversion single-photon detector. *Opt. Commun.* **2016**, *381*, 37–42. [CrossRef]
13. Shangguan, M.; Wang, C.; Xia, H.; Shentu, G.; Dou, X.; Zhang, Q.; Pan, J.-W. Brillouin optical time domain reflectometry for fast detection of dynamic strain incorporating double-edge technique. *Opt. Commun.* **2017**, *398*, 95–100. [CrossRef]
14. Belmekki, M.A.A.; Leach, J.; Tobin, R.; Buller, G.S.; McLaughlin, S.; Halimi, A. 3D target detection and spectral classification for single-photon LiDAR data. *Opt. Express* **2023**, *31*, 23729–23745. [CrossRef]
15. Maccarone, A.; McCarthy, A.; Ren, X.; Warburton, R.E.; Wallace, A.M.; Moffat, J.; Petillot, Y.; Buller, G.S. Underwater depth imaging using time-correlated single-photon counting. *Opt. Express* **2015**, *23*, 33911–33926. [CrossRef]

16. Maccarone, A.; Della Rocca, F.M.; McCarthy, A.; Henderson, R.; Buller, G.S. Three-dimensional imaging of stationary and moving targets in turbid underwater environments using a single-photon detector array. *Opt. Express* **2019**, *27*, 28437–28456. [CrossRef] [PubMed]
17. Shen, X.; Kong, W.; Chen, P.; Chen, T.; Huang, G.; Shu, R. A shipborne photon-counting lidar for depth-resolved ocean observation. *Remote Sens.* **2022**, *14*, 3351. [CrossRef]
18. Shangguan, M.; Liao, Z.; Guo, Y.; Lee, Z. Sensing the profile of particulate beam attenuation coefficient through a single-photon oceanic Raman lidar. *Opt. Express* **2023**, *31*, 25398–25414. [CrossRef] [PubMed]
19. Wang, J.; Hao, W.; Chen, S.; Zhang, Z.; Xu, W.; Xie, M.; Zhu, W.; Su, X. Underwater single photon 3D imaging with millimeter depth accuracy and reduced blind range. *Opt. Express* **2023**, *31*, 30588–30603. [CrossRef]
20. Zhou, Y.; Chen, Y.; Zhao, H.; Jamet, C.; Dionisi, D.; Chami, M.; Di Girolamo, P.; Churnside, J.H.; Malinka, A.; Zhao, H.; et al. Shipborne oceanic high-spectral-resolution lidar for accurate estimation of seawater depth-resolved optical properties. *Light Sci. Appl.* **2022**, *11*, 261. [CrossRef]
21. Shangguan, M.; Guo, Y.; Liao, Z. Shipborne single-photon fluorescence oceanic lidar: Instrumentation and inversion. *Opt. Express* **2024**, *32*, 10204–10218. [CrossRef]
22. Maccarone, A.; Drummond, K.; McCarthy, A.; Steinlehner, U.K.; Tachella, J.; Garcia, D.A.; Pawlikowska, A.; Lamb, R.A.; Henderson, R.K.; McLaughlin, S.; et al. Submerged single-photon LiDAR imaging sensor used for real-time 3D scene reconstruction in scattering underwater environments. *Opt. Express* **2023**, *31*, 16690–16708. [CrossRef]
23. Halimi, A.; Maccarone, A.; McCarthy, A.; McLaughlin, S.; Buller, G.S. Object Depth Profile and Reflectivity Restoration From Sparse Single-Photon Data Acquired in Underwater Environments. *IEEE Trans. Comput. Imaging* **2017**, *3*, 472–484. [CrossRef]
24. Wang, J.; Hao, W.; Chen, S.; Xie, M.; Li, X.; Shi, H.; Feng, X.; Su, X. Underwater Single-Photon Profiling Under Turbulence and High Attenuation Environment. *IEEE Geosci. Remote Sens. Lett.* **2024**, *21*, 1–5. [CrossRef]
25. Deng, R.; He, Y.; Qin, Y.; Chen, Q.; Chen, L. Measuring pure water absorption coefficient in the near-infrared spectrum (900–2500 nm). *J. Remote Sens.* **2012**, *16*, 192–206. [CrossRef]
26. Laux, A.; Billmers, R.; Mullen, L.; Concannon, B.; Davis, J.; Prentice, J.; Contarino, V. The a, b, c s of oceanographic lidar predictions: A significant step toward closing the loop between theory and experiment. *J. Mod. Opt.* **2002**, *49*, 439–451. [CrossRef]